



Losses in magnetic field resilient coplanar stripline resonators

Downloaded from: <https://research.chalmers.se>, 2025-06-15 11:20 UTC

Citation for the original published paper (version of record):

Cools, I., Trnjanin, N., Buccheri, V. et al (2025). Losses in magnetic field resilient coplanar stripline resonators. *Journal of Physics D: Applied Physics*. <http://dx.doi.org/10.1088/1361-6463/added5>

N.B. When citing this work, cite the original published paper.

PAPER • OPEN ACCESS

Losses in magnetic field resilient coplanar stripline resonators

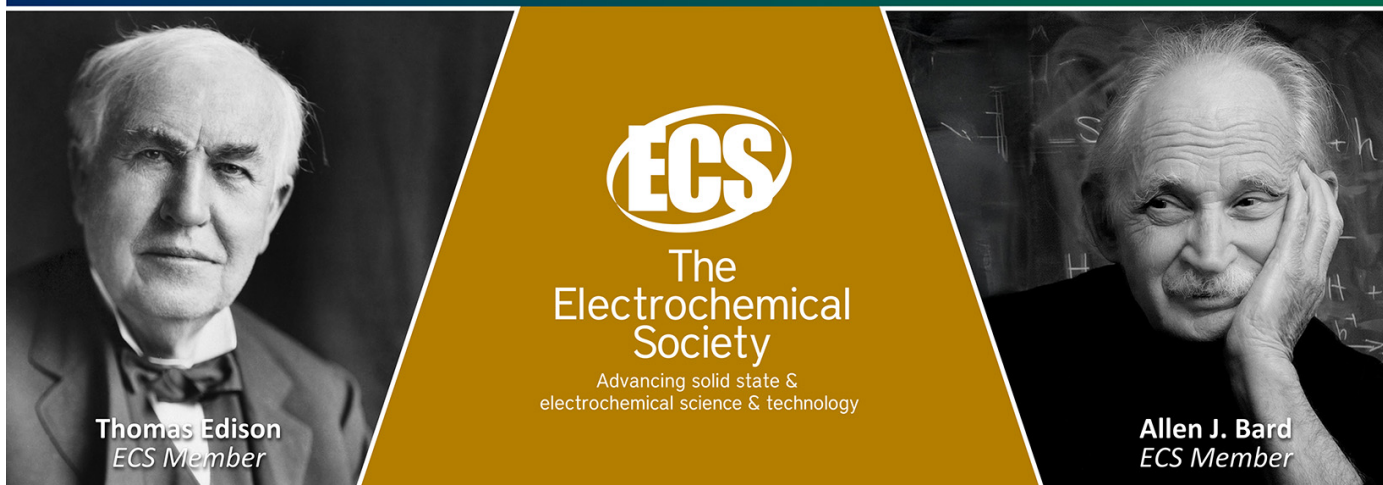
To cite this article: Ivo P C Cools *et al* 2025 *J. Phys. D: Appl. Phys.* **58** 255102

View the [article online](#) for updates and enhancements.

You may also like

- [Evaluation of a microplasma source based on a stripline split-ring resonator](#)
M Berglund, M Grudén, G Thornell et al.
- [Nanoscale microwave imaging with a single electron spin in diamond](#)
Patrick Appel, Marc Ganzhorn, Elke Neu et al.
- [Beam position monitor design for the High Energy Photon Source](#)
Jun He, Yanfeng Sui, Yong Li et al.

Join the Society
Led by Scientists,
for *Scientists Like You!*



Thomas Edison
ECS Member

ECS
The
Electrochemical
Society
Advancing solid state &
electrochemical science & technology

Allen J. Bard
ECS Member

Losses in magnetic field resilient coplanar stripline resonators

Ivo P C Cools* , Rodrigo M López-Báez , Vittorio Buccheri ,
Oleg Shvetsov , Nermin Trnjanin , Emil Hogedal  and Saroj P Dash 

Department of Microtechnology and Nanoscience, Chalmers University of Technology, SE-41296 Gothenburg, Sweden

E-mail: Cools@chalmers.se

Received 26 February 2025, revised 23 May 2025

Accepted for publication 30 May 2025

Published 11 June 2025



CrossMark

Abstract

Coplanar waveguide (CPW) resonators have shown considerable success in circuit quantum electrodynamics research. However, their susceptibility to an external magnetic field limits their general functionality. In addition, electrical voltage gating for devices coupled to a CPW resonator necessitates alterations to the ground plane, changing the resonator characteristics. To avoid these problems, we fabricated and measured quarter wavelength differentially driven coplanar stripline (CPS) resonators made of NbTiN. We measured multiple devices with varying geometrical parameters in these novel resonators and analyse changes in their internal quality factor and two-level system losses. Furthermore, we establish the resilience of the resonators to an applied magnetic field by tracking the resonance frequency shift, without optimisation of the resonator geometry. Due to their flexible design and high magnetic field resilience, CPS resonators are particularly well-suited to study superconductor-semiconductor heterophysics where voltage gating or a magnetic field are necessary.

Keywords: resonator, quantum computing, Andreev bound states, superconductor, quantum information

1. Introduction

In recent years, superconducting microwave resonators have garnered significant attention in the field of circuit quantum electrodynamics (cQEDs) for their ability to enable precise readout and manipulation of qubits [1–3]. Among the various geometries used in this field, coplanar waveguide (CPW) resonators have emerged as the workhorse due to their ease of fabrication and high internal quality factors (Q_i) [4, 5].

These distributed element resonators consist of a single central conducting transmission line, separated from a ground plane carrying a return current, and are usually fabricated from a superconducting material (e.g. Al, Nb, NbTiN...). In cQED, the coupling strength between resonator and the dipolar moment of hybrid superconductor-semiconductor structures, such as electrons in single or double quantum dots [6–8], electronic spins [9, 10] or quasiparticles in semiconductors [11] can be tunable. It is mediated by the zero point voltage fluctuations $V_{ZPF} \sim \omega_R \sqrt{Z_R}$ in the resonator, where ω_R is the angular fundamental resonance frequency and $Z_R = \sqrt{\frac{L_R}{C_R}}$ is the characteristic impedance of the resonator as defined by the resonator's inductance, L_R , and capacitance, C_R . Hence, to achieve the strong coupling regime it is typically necessary to fabricate the device from a superconducting material with high kinetic inductance. Such applications often require electrostatic gating, which necessitates the interruption of the ground plane particularly when gating multiple devices per resonator.

* Author to whom any correspondence should be addressed.



Original Content from this work may be used under the terms of the [Creative Commons Attribution 4.0 licence](https://creativecommons.org/licenses/by/4.0/). Any further distribution of this work must maintain attribution to the author(s) and the title of the work, journal citation and DOI.

This alteration changes the characteristics of a CPW as it disturbs the return current flowing through the ground plane [12, 13], which requires significant alterations to the microwave environment or design [14]. Moreover, this introduces electromagnetic interference problems, such as the appearance of parasitic slotmodes [15]. Additionally, applications frequently require an externally applied magnetic field, which leads to the formation of vortices in the ground plane, resulting in energy dissipation [4, 16, 17].

A native approach to avoid these problems is to omit the interfering ground plane altogether and use a coplanar stripline (CPS) geometry. In this regard, we fabricated and measured differentially driven $\lambda/4$ CPS resonators made from 10 nm thick sputtered NbTiN (with kinetic inductance $L_K \cong 10 \text{ pH}/\square$). We start this paper by demonstrating the consistency of this novel type of resonator, shown by corresponding measurement and simulation results. We study in detail the different microwave loss mechanisms by varying geometrical parameters of the resonators. Both dependence on the width of the resonator prongs and the evolution of loss under an increasing prong-spacing are investigated. These geometrical parameters determine partially the losses in the resonator [18]. By examination of the power dependence of Q_i of each resonator together with a temperature dependence of the resonance frequency, insight is provided into the spectral distribution of two-level system (TLS) losses. This large variation in parameter space allows us to characterise resonators with impedances ranging from 81 to 681Ω , using a film with a relatively low kinetic inductance compared to similar measurements from high-impedance resonators in literature [19–21]. Finally, from the behaviour of the resonators in magnetic field, film parameters such as the electronic diffusion coefficient are determined.

2. Fabrication

The resonators are fabricated on double side polished $430 \pm 25 \mu\text{m}$ thick C-plane Al_2O_3 wafers. In a first step, these wafers are cleaned using a standard 5:1:1 RCA process of respectively deionised water, ammonia water and H_2O_2 , heated to 80°C for 10 min [22]. Subsequently both sides of the wafer are covered by sputtering on a target of $\text{Nb}_{81.9}\text{Ti}_{18.1}\text{N}$ in a near-UHV sputter system from DCA instruments [23], using an Ar:N₂ partial gas pressure ratio of 60:37. On the wafer's backside, approximately 100 nm of NbTiN is sputtered. During this stage of the fabrication process, the wafer is actively cooled with a cooling element. After a brief, *ex-situ* cleaning step with isopropyl alcohol, NbTiN is deposited on the sample-side of the sapphire: first, the wafer is pre-annealed at 660°C for 30 min and then sputtered with NbTiN for 34 s. Subsequently, the CPS resonators are patterned on the sample side via e-beam lithography using a HSQ negative resist mask, pre-baked at 90°C . An e-spacer 300Z conduction layer is applied to mitigate substrate charging. After development for 60 s in MF319, an Ar/Cl (4:50 sccm)

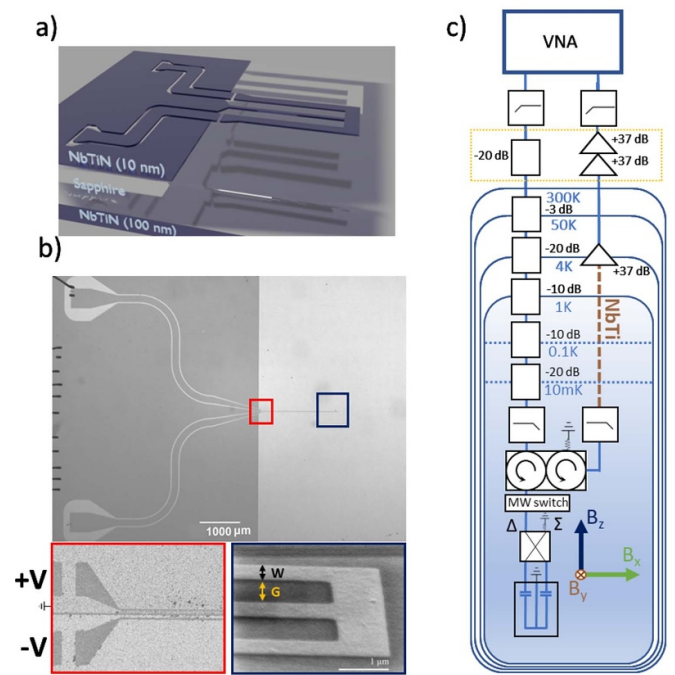


Figure 1. Experimental setup and sample specifics. (a) Schematic view of the sample stack. (b) Optical image of one resonator. Inset are SEM images of the capacitive gap coupler (red) and the resonator's end (dark blue), the latter visualising the definition of lead width W and gap G . (c) The dilution refrigerator and room-temperature microwave setup for the experiments. Elements enclosed in the yellow-dashed lines are only used for low-power measurements (below -30 dBm applied VNA power) to avoid resonator bifurcation at high powers.

ICP plasma etches the unwritten part of the metal [24, 25]. Finally, the HSQ is removed by a 30 s dip in a 2% HF solution. The final stack is shown in figure 1(a). After dicing, the sample is pasted using standard silver paint to the bottom of an oxygen free copper box, used for its high thermal conductivity at low temperatures [26]. Finally, it is bonded using Al/Si bondwires to a PCB.

3. Methods

Shown in figure 1(b) is an optical image of one of the resonators. A CPW feedline is used to route the signal from the PCB to the CPS resonator to minimise impedance mismatch. The CPS is connected to this feedline via standard in-plane gap coupling capacitors (bottom left inset in figure 1(b)). We stress here that our CPS geometry does not involve a coplanar ground plane. This enables the potential use of gating structures near the resonator without significantly altering its characteristics, an area typically reserved for the groundplane in a CPW geometry. Furthermore, due to the differential drive of the CPS, a grounding strip line at zero-point DC voltage can be implemented to DC-ground coupled electrostatically sensitive structures. The presently shown resonators include this ground line to more accurately mimic a realistic measurement

scenario. To keep the fundamental odd resonance frequency at 6 GHz, the total length of each resonator is adjusted following simulation in Sonnet, necessitated by the variations in geometrical parameters (resonator lead width W and lead spacing G , as illustrated in a scanning electron microscope image 1(b), bottom right inset). Via similar simulations, we estimate the external quality factor Q_C by estimations of the resonance frequency bandwidth using a lossless dielectric [4].

The devices are measured in a BlueFors LD dilution refrigerator, with base temperature ~ 10 mK, using a setup as shown in figure 1(c). The VNA, a Keysight P5004A, is protected from DC signals by a high-pass filter (Mini-Circuits BLKD-183-S + DC block) on both input and output sides. The probing signal is attenuated at the different temperature stages to achieve an upper bound of 10^{-3} noise photon number at the mixing chamber plate [27]. Besides the cryogenic attenuators, we assume an extra 6 dB attenuation from the CuNi coaxial microwave cabling [27, 28]. To further minimise stray infrared radiation causing quasiparticle generation [29], two in-house fabricated copper powder filters [30, 31] are mounted at the mixing chamber plate, both on the input and output side, with cut-off frequency at ~ 18 GHz. A dual circulator-isolator (LNF-CIISC4_12A) routes the signal first to through a six-port microwave switch (Radiall Cryogenic SP6T switch) to the Δ -port of a 180° -hybrid (Krytar 4060 200) which splits the signal, allowing to differentially drive the resonator through two short phase-matched SMA cables between hybrid and sample. The reflected signal from the resonating sample is routed to an output line where a cryogenic low noise amplifier (LNF-LNC4_16B mounted at the 4 K stage) and two room-temperature HEMT low noise amplifiers (LNF-LNR4_14B) amplify the outgoing signal. Physically the resulting measurement is between ports 1 and 2 of the VNA (S_{21} -spectrum), yet due to the presence of the circulator in the measurement setup has to be seen as a reflection measurement of the resonator (S_{11} -spectrum). Magnetic field reliant data is measured in a similar dilution refrigerator but containing a vector magnet (AMI Cryogen-free MAxis Vector Magnet).

We use this setup to investigate the effect of varying W and G on the resonator losses in both power and temperature. Figures 2(a) and (b) show representative data in a small frequency window around the resonance frequency f_R of the resonator with $W = 1 \mu\text{m}$ and $G = 10 \mu\text{m}$. Both a representative normalised $|S_{11}|$ plot and the normalised data represented in the IQ-plane are shown. Reflection data is fitted around the fundamental odd resonance using the diameter-correction method [32, 33], taking into account the fact that the resonators are purely reflectively measured (and thus not hanger-type). In that case, we describe S_{11} as [34]:

$$S_{11} = ae^{i\alpha} e^{-2\pi i f_R \tau} \left(1 - \frac{2Q_i}{\widetilde{Q}_c} \frac{1}{1 - 2iQ_i \left(\frac{f_R - f}{f_R} \right)} \right). \quad (1)$$

Here, the prefactor $ae^{i\alpha} e^{-2\pi i f_R \tau}$ is due to the resonator's environment: a is the attenuation factor of the signal, $e^{i\alpha}$ acts as a phase prefactor and $e^{-2\pi i f_R \tau}$ is due to the electrical delay

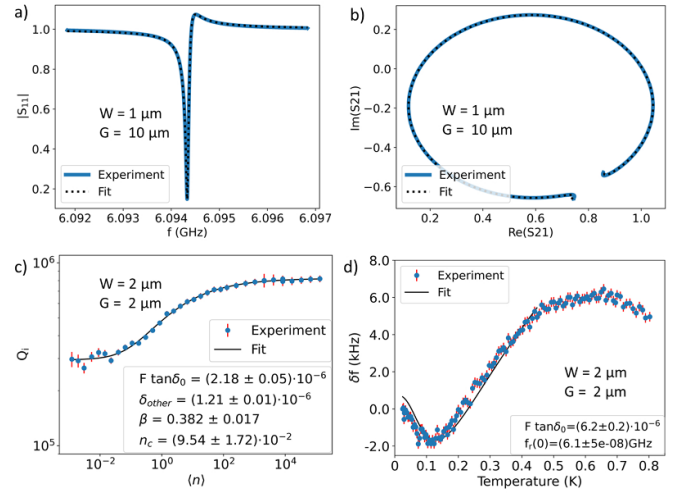


Figure 2. Representative fits and plots of the losses of coplanar stripline resonators. (a) Normalised $|S_{11}|$ versus frequency for the resonator with width $W = 1 \mu\text{m}$ and gap $G = 10 \mu\text{m}$. Experimental data (blue) is fitted to equation (5) (black dashed line). (b) The resonator of (a), plotted in the IQ-plane, showing the effect of the impedance miss-match near the off-resonance point. (c) A representative power-dependent evolution of the internal quality factor of the resonator with $W = 2 \mu\text{m}$ and $G = 2 \mu\text{m}$. The experimentally determined internal quality factor Q_i values (blue), including error bar (red), are fitted to equation (5) (black). (d) Low-temperature dependent resonance shift at zero magnetic field at high average internal photon level. The experimentally determined frequency shift δf values (blue), including error bar (red), are fitted to equation (6) (black).

in the refrigerator's microwave lines. Furthermore, Q_i is the total quality factor, combining both Q_i , the internal and the complex external quality factor $\widetilde{Q}_c = |Q_c| \exp(-i\phi)$ as $Q_i^{-1} = Q_i^{-1} + Q_c^{-1}$. This complex Q_c describes the asymmetry in the Lorentzian line shape of $|S_{11}|$ and is attributed to either an impedance mismatch [4], an extra series inductance from the wire bond connections [35, 36] or even reflections in the resonator's feedline [37]. For the data in the IQ-plane, the mismatch exhibits itself as non-circular behaviour near the off-resonance point. Simulation in the open-source software package QUCS [38] hints towards a phase-mismatch of the cables after the hybrid as a potential source of this ϕ -factor (appendix D). For the dataset shown in figures 2(a) and (b), the mismatch is $\phi = -0.43$. Fitting scripts are available on the group's GitHub page [39].

To verify whether standard CPW resonator routines (e.g. simulation) work for differentially driven CPS resonators, we present the data in figure 3. When fabricating a sample, we measure the DC sheet resistance of the NbTiN film which allows us to estimate the kinetic inductance via equation [40] 2:

$$L_k(T = 0\text{K}) = \frac{\hbar R_N}{\pi \Delta_0}, \quad (2)$$

where we use the superconducting energy gap of NbTiN via the BCS theory for extremely dirty superconductors: $\Delta_0 =$

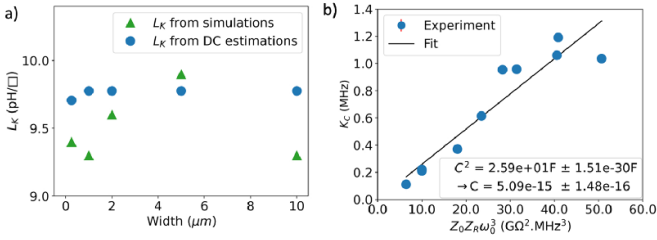


Figure 3. (a) The estimated kinetic inductance L_K of each sample from DC measurement of bulk films at room temperature, compared to the estimated kinetic inductance from simulations of the resonance in the mK regime. Green triangles are the simulated L_K , blue circles are the estimated L_K from DC measurements. (b) Validity test of the simulation and fitting procedures. The external quality factor Q_c is plotted versus the rescaled simulated impedance of the resonators. A fit is performed using equation (3).

$1.764k_B T_c$ [41–43]. The critical temperature T_c is estimated from previous DC measurements on NbTiN films of the same thickness (15.2 K), while the normal state resistance R_N is ideally measured right above T_c . As the resistance of disordered metals does not change appreciably with temperature, we estimate it from measurements at room temperature. All DC parameters of a representative film are shown in appendix A. We correspond the resulting inductance value to the kinetic inductance we obtain from a comparison between a simulated resonance frequency in Sonnet to the fitted resonance frequency from measurements [21]. This data is shown in figure 3(a). We attribute deviations to fabrication tolerances, a slight non-uniformity of the film thickness and the crude estimation of the kinetic inductance using only the room-temperature sheet resistance. A second check of simulations versus measurements is shown in figure 3(b). From fitting resonator data we obtain the external quality factor Q_c while from resonator simulations we obtain its impedance Z_R . The relation between Q_c and Z_R is (derived in appendix B)

$$Q_c = \frac{\pi}{4(2\pi f_R)^2 C_c^2 Z_0 Z_R}. \quad (3)$$

This allows us to derive the coupling capacitance C_c . In the resonator designs, this capacitance was kept approximately constant. However, deviations cause discrepancies between data and fit, e.g. due to the increasing width of the conductor which changes C_c but was unaccounted for. Furthermore, a constant f_R was assumed, but here a natural variation due to slightly differing kinetic inductances was also observed. Finally, at smaller resonator conductor width, fabrication errors become relatively more pronounced (i.e. at higher Z_R). We use equation (3) to do a linear fit to the coupling rate $\kappa_c = \frac{2\pi f_R}{Q_c}$ in function of $Z_R f_R \times Z_0 f_R^2$ to obtain the coupling capacitance directly, and we get a reasonable value of $C_c = (5.09 \pm 0.148) \times 10^{-15}$ F. We find the correspondence enough to conclude that standard industry CPW simulation and fitting routines are applicable to CPS resonators.

4. Losses

To understand the behaviour of TLS losses on the resonator, the evolution of Q_i on input power is studied at base refrigerator temperature. As input power varies depending on the exact attenuation, the unitless quantity of average photon number $\langle n \rangle$ is used instead, defined as [44, 45]:

$$\langle n \rangle = \frac{4}{2\pi} \frac{Z_0}{h f_R^2} \frac{Q_i^2}{Z_R Q_c} P_{\text{IN}} \quad (4)$$

where both the characteristic impedance of the input feedline, Z_0 , as that of the resonator Z_R play a role as well as the input power P_{IN} at the resonator's feedline. At low temperature, we fit the power-dependent Q_i to [45, 46]:

$$\frac{1}{Q_i} = \frac{F \tan(\delta_{\text{tls}}^0)}{\left(1 + \frac{\langle n \rangle}{n_c}\right)^\beta} + \delta_{\text{other}} \quad (5)$$

where F is a material dependent filling factor of the electric field [45], $\tan(\delta_{\text{tls}}^0)$ the intrinsic TLS loss tangent of the same material, and δ_{other} is usually dominated by the next-largest loss channel of the resonator. Furthermore, the amount of photons needed to saturate the TLS is given by n_c , while β is determined by the interacting strength between individual TLS. For non-interacting TLS [47], β equals 0.5. We neglect the effect of quasiparticles with increasing μW -power [12, 48] due to the comparatively low kinetic inductance fraction in these resonators [49] and the presence of low-pass copper powder filters filtering away high energy radiation. A representative fit is shown in figure 2(c). In this plot, the difference between high and low power saturation values is attributed to the TLS losses. Since this power-dependence approach only probes a narrow window of TLS around the resonance, they are called the *narrow-band TLS losses*. [50, 51]. At higher power, the intrinsic kinetic inductance of the resonator causes a bifurcation, likely a Duffing non-linearity [52], complicating the fitting procedure. We do not include these points in our fit, as a full description is outside the scope of this paper.

On the other side, the *wide band TLS losses* are uncovered by the temperature dependence of the real part of the dielectric constant, usually measured via the shift in relative resonance frequency up until ~ 1 K [47, 53]:

$$\delta f = \frac{\Delta f}{f_0} = \frac{k}{\pi} \left(\text{Re} \left[\Psi \left(\frac{1}{2} + \frac{1}{2\pi i} \frac{h f_R(T)}{k_B T} \right) \right] - \ln \left(\frac{h f_R(T)}{k_B T} \right) \right). \quad (6)$$

Here is $\Delta f = f_R(T) - f_0$ the temperature-dependent resonance frequency referenced at low temperature (in our data at 10 mK) while Ψ is the complex digamma function. The factor $k = F \delta_{\text{tls}}^{0,i}$ contains the intrinsic temperature dependent TLS-loss component, $\delta_{\text{tls}}^{0,i}$, which is sensitive to thermally varying TLS for a wide spectrum [24].

As these off-resonant TLS are not saturated, the frequency shift is nearly power independent and it is possible to gather data at higher powers which speeds up measurements. We used

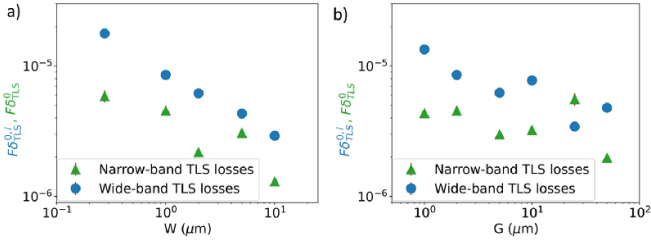


Figure 4. The evolution of the geometrically dependent loss tangent of the narrow-band losses $F_{\text{tls}}^{\text{nb},0}$ (green triangles) and the wide-bands losses $F_{\text{tls}}^{\text{wb},0,i}$ (blue circles) (a) decreases with increased width W of the resonator leads (for constant gap spacing $G = 2 \mu\text{m}$) and (b) decreases with an increasing G of the leads (for constant $W = 1 \mu\text{m}$).

$\langle n \rangle = 1e5$, which for each resonator is in the high-power saturated regime [51]. At higher temperatures, the onset of quasiparticles dominates the resonator's frequency shift and losses [21, 54]. For this reason we constrained our fits to data up to 450 mK, still well below the superconducting energy gap of NbTiN. A representative fit of the temperature dependent frequency shift is shown in figure 2(d). The presence of a universal dip in the relative frequency shift at $T \approx \frac{\hbar\omega_R}{2k_B}$ supports the validity of equation (6) for these resonators, and confirms that quasiparticle loss is not a dominant factor in the total loss of the resonator [49, 55]. The observed discrepancy between fit and experimental data at very low temperatures has similarly been observed for TLS-dominated CPW resonators [56, 57].

Using the established fitting and simulation procedure, we quantify the losses depending on resonator lead geometry using the aforementioned methods (power and temperature dependence, with fits to resp. Equations (5) and (6)). As shown in figure 4, we observe decreasing losses with both W -dependence of the lead as with G , which is on the same order of magnitude as results of similar geometric dependences of CPW resonators [4, 53, 58, 59]. We report the data of all devices numerically in appendix C. We explain the geometric behaviour by the fact that the current density (and hence electric field) is highest on the inner edges of the differentially driven resonators [60, 61]. This means that the interaction of the field with the TLS is enhanced there and thus TLS losses are higher for resonators with a relatively larger contribution of conductor-edge to total-resonator-surface. These are the narrower resonators, as the data shows. In a similar vein, an increased gap to lead-width ratio decreases the current density at the inner edge and improves the TLS losses.

We support this conclusion by the simulations of interface participation ratios p_i shown in figure 5(a). This entity describes how much of the electrical field is threaded through each individual volume in the resonator. As electric field couples to the dipolar TLS, a higher participation ratio leads to a relatively larger loss for a given volume. We describe these ratios by the penetrating of the field through four dielectric regions: metal-air (ma), metal-substrate (ms), substrate-air (sa) and substrate. Here, we neglect the influence of the participation ratio of the perfect vacuum volume. More details on the simulation are given in appendix F. The metal-air interface

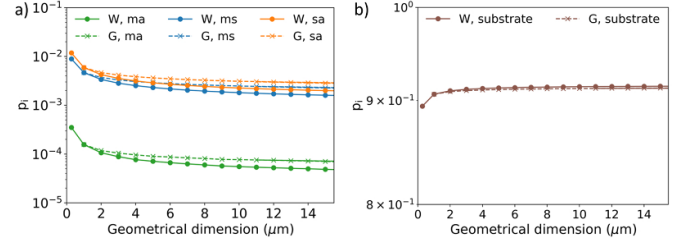


Figure 5. Simulation of the participation ratios of different dielectric volumes of the resonators. (a) Simulation of the metal-air (ma), metal-surface (ms) and surface-air (sa) interfaces, threaded by the electric field and their evolution with geometrical parameter (resp. W , width, in full line and circle, and G , the gap, in dashed line and cross). (b) Simulation of the participation ratio of the substrate and its evolution with geometrical parameter.

has two orders of magnitude less contribution to loss participation than both the ms and the sa interfaces, including at higher dimensions of both width and gap. As the participation ratio of the lossy dielectric interfaces drop for larger geometrical dimension, the relative contribution of the substrate related losses increase as shown in figure 5(b). This is because the total electrical field penetrating the ms and ma interfaces scale as approximately respectively W or G while the total field in the substrate scales as approximately W^2 and G^2 . Since the losses of bulk sapphire are negligible compared to those in the resonator surfaces (the bulk average losses of sapphire are in the range of $10^{-7} - 10^{-9}$, while those of the resonator surfaces are around $10^{-3} - 10^{-4}$), the overall internal quality factor decreases with increasing width and gap as observed [62, 63].

5. Magnetic field dependence

The behaviour of the resonance frequency to a magnetic field is shown in figure 6. These measurements were taken at an average photon number of $\langle n \rangle \sim 10^4$. The thick substrate effectively shields the resonator current distribution from the effect of vortex nucleation on the superconducting plane on the sample's backside [60]. Hence, the magnetic field behaviour is fully due to the currents circulating in the resonator leads. In general, the relative frequency shift due to the supercurrent depairing by a parallel magnetic field is well approximated by a quadratic relation of the form

$$\frac{\Delta f_R(B)}{f_{R,0}} = -k_{\parallel} B_{\parallel}^2 \quad (7)$$

$$= \frac{-\pi}{48} \frac{De^2}{\hbar k_B T_c(0)} B_{\parallel}^2 t^2, \quad (8)$$

valid for thin films where the t is much smaller than the *effective* London penetration depth, $\lambda_{\text{eff}} = \lambda(1 + \frac{\xi_0}{l})^{\frac{1}{2}}$, around $1 \mu\text{m}$ for these films [43, 64–67]. Here, λ , ξ_0 and l are respectively the London penetration depth, the coherence length of NbTiN and the elastic electron mean free path, for which representative values are shown in appendix A.

We extend this formalism to a perpendicular magnetic field. In that case [68], as $t \ll \lambda_{\text{eff}}$, the screening distance

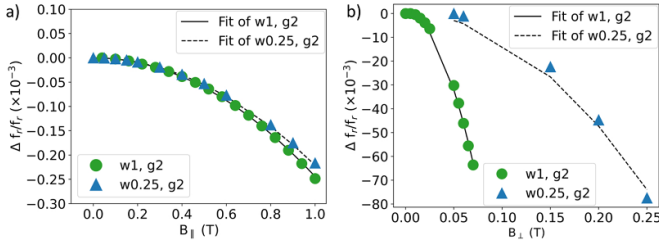


Figure 6. The relative shift of the resonance frequency of the resonator with width $W = 0.25 \mu\text{m}$ and $1 \mu\text{m}$ (gap spacing $G = 2 \mu\text{m}$) when sweeping an external magnetic field. Error bars are smaller than the data points. (a) and (b) Evolution of the frequency shift under an in-plane (perpendicular) applied field. Data is fit to $\frac{\Delta f/f_r}{f_r} = -k_{\parallel(\perp)} B_{\parallel(\perp)}^2$.

takes the form of $\lambda_{\perp} = \frac{\lambda_{\text{eff}}^2}{t} \approx 100 \mu\text{m} \gg W$. This validates our approach to use W instead of t for perpendicular fields in equation (8). For the data shown in figure 6, we get $k_{0.25\mu\text{m},\perp} = 1.18 \pm 4.81 \times 10^{-2} \text{ T}^{-2}$ and $k_{1\mu\text{m},\perp} = 1.28e1 \pm 1.37 \times 10^{-1} \text{ T}^{-2}$. In this approximation, we can derive directly the electron diffusion coefficient D of the NbTiN films. We obtain diffusion coefficients of $D_{1\mu\text{m}} = 1.55 \text{ cm}^2 \text{ s}^{-1}$ and $D_{0.25\mu\text{m}} = 2.29 \text{ cm}^2 \text{ s}^{-1}$ from the perpendicular field data, which is in line with earlier reported results on NbTiN [19, 20, 65, 69].

We use these derived diffusion coefficients of the material to recreate the effective electronic thickness of the film. For this, we determine the k -values of the devices under an in-plane applied magnetic field parallel to the resonator direction with equation (8). We extract respective k -values of $k_{0.25\mu\text{m},\parallel} = 2.23 \times 10^{-4} \pm 4.0 \times 10^{-7} \text{ T}^{-2}$ and $k_{1\mu\text{m},\parallel} = 2.47 \times 10^{-4} \pm 3.74 \times 10^{-7} \text{ T}^{-2}$, which results in calculated electronic film thicknesses of 4.39 nm and 3.44 nm for the $1 \mu\text{m}$ and 250 nm wide resonators, respectively. We attribute the difference to the physical layer thickness to rough granular structure of the NbTiN, especially near the substrate surface, and the suppression of shielding currents within one coherence length from the surfaces. Finally, we stress the resonator's reliability in magnetic field from the consistent and low relative resonance frequency shift up to 1 T for a parallel field and up to 250 mT for a perpendicular field.

6. Summary

In conclusion, this paper presented the fabrication and characterisation of differentially driven CPS superconducting resonators with varying geometrical parameters, made from a $10 \text{ pH}/\square$ NbTiN layer. By varying the width of the conductor leads and the spacing between the conductor pair, we achieved impedances ranging from 81 to 681Ω . This stresses the flexibility of the CPS as its impedance is proportional to the coupling strength with a dipolar moment of e.g. Andreev bound states in semiconducting nanowires [70]. Moreover, the lack of groundplane makes these resonators an ideal platform for the next generation of superconductor-semiconductor heterostructure coupled devices, as they enable electrostatic gating without compromising resonator characteristics. Through the

use of standard fitting techniques, we determined that losses are dominated by TLS in the zero-field regime. Furthermore, magnetic field indicates a high electronic diffusion constant of the NbTiN films, suggesting a high film quality. The films are especially resilient to parallel magnetic fields, which are paramount for cQED Majorana research. Future work includes incorporating semiconductor nanostructures into these resonators to directly measure the spectrum of an Andreev molecule.

Data availability statement

The data cannot be made publicly available upon publication because they are not available in a format that is sufficiently accessible or reusable by other researchers. The data that support the findings of this study are available upon reasonable request from the authors.

Acknowledgments

Devices were fabricated in the Myfab cleanroom Chalmers, and we acknowledge the help we got from Nanofabrication Laboratory engineers. We have gained a lot from useful discussions with V Fatemi, T Connolly, S Mahashabde, F Joint, D Winkler and B Dalelkhan. L Jönsson's help was invaluable to fabricate sample boxes and in other mechanical help. I P C C, V B and N T acknowledge support by the European Union's H2020 research and innovation program, grant no. 804988 (SiMS) and 828948 (AndQC). We gracefully acknowledge A Geresdi in obtaining this funding.

Conflict of interest

The authors have no conflicts to disclose.

Appendix A. DC characterisation

We performed DC characterisations of our NbTiN films in a four-point Hall bar geometry, with channel width $10 \mu\text{m}$, length $595 \mu\text{m}$ and specifically fabricated out of the same film as the resonator with both width and gap $2 \mu\text{m}$. All DC results are summarised in figure 7. We first measure the critical temperature T_c of the nominally $d = 10 \text{ nm}$ thick film. In figure 7(a), we show the $R(T)$ plot taken by cooling the sample from room temperature (bias 100 nA) to base temperature (2 K) in a Quantum Design DynaCool PPMS. From the data we obtain $R_n = 98.3 \Omega/\square$ (near T_c) and a critical temperature of 15.2 K . To estimate this T_c we use a $1 \Omega/\square$ cut-off. Subsequently, shown in figure 7(b), we perform Hall measurements. This happens at 30 K to avoid potential interference of superconducting current screening. We again use a current-biased four-point measurement scheme with $I = 25 \mu\text{A}$ to measure the Hall-voltage $V_H(B)$. Furthermore, we account for a small voltage offset of $1.2 \mu\text{V}$, likely due to fabrication errors in the Hall bar (misalignment of the arms). A linear fit to the

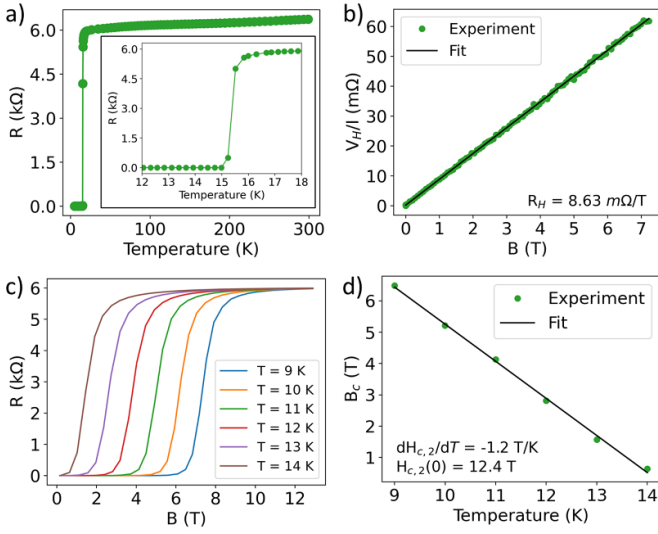


Figure 7. DC measurement data of our nominally 10 nm thick NbTiN films. (a) $R(T)$ plot, taken in decreasing temperature, with the insert showing a finer scan (increasing temperature) around $T_c = 15.2$ K. (b) Current biased (25 μ A) Hall measurement to extract the Hall-coefficient. Via a linear fit we extract $R_H = 8.62$ $m\Omega T^{-1}$. (c) Small subset of the $B(T)$ -phase diagram for the film. We use a 1 Ω/\square cut-off to estimate the critical magnetic field B_c at every fixed temperature. (d) The estimated critical fields in function of the temperature near T_c . A fit to equation (A1) data generates $H_{c,2}(0) = 12.4$ T and $\frac{dH_{c,2}}{dT} = -1.2$ T K^{-1} .

data gives a Hall coefficient of $R_H = 8.63$ $m\Omega T^{-1}$. This coefficient is also defined as $R_H = \frac{1}{n_e e d}$; hence we obtain consecutively the electron carrier density $n_e = 7.23 \times 10^{28}$ m^{-3} and the Fermi wave vector $k_F = (3\pi^2 n_e)^{\frac{1}{3}} = 12.9$ nm^{-1} from the Hall measurement. Finally, we derive the elastic electron mean free path $l_e = \frac{\hbar k_F}{n_e e^2 R_H d} = 0.74$ nm, a value similar to other NbTiN films reported in literature [65].

To extract the NbTiN coherence length, we first measure a $B(T)$ diagram under a constant applied current bias of 25 nA, shown in figure 7(c). By scanning the magnetic field at fixed temperatures, we obtain the critical magnetic field B_c for each. Again, we use a 1 Ω/\square cut-of criterion. The close-to- T_c tail-end of the B_c 's is shown in figure 7(d). Here, we can extract the critical field at 0 K for a type-II superconductor from fitting the data to the Werthamer-Helfand-Hohenberg formula [71]

$$B_{c,2}(0) = -\ln(2) T_c \left(\frac{dB_{c,2}}{dT} \right)_{T=T_c}. \quad (A1)$$

Using our initially measured $T_c = 15.2$ K, this gives $B_{c,2} = 12.4$ T. As the last step, we derive the Ginzburg–Landau coherence length as $\xi(0) = \sqrt{\frac{\phi_0}{2\pi B_{c,2}(0)}}$, giving $\xi(0) = 5.1$ nm.

Appendix B. Qc in Zr derivation

To derive equation (3), we followed the same procedure as [20], but adapted to pure reflection type $\lambda/4$ -resonators. The input impedance of a shorted $\lambda/4$ line is given by [72]

$$Z_{in} = \frac{2Z_R}{\frac{\pi}{2Q_i} + \frac{i\pi\Delta\omega_0}{\omega_0}} \quad (B1)$$

where Z_R is the resonator's characteristic impedance and $\Delta\omega_0$, the drive frequency ω offset to the bare resonator resonance frequency ω_0 . Coupling the resonator to the environment is usually done via a coupling capacitance C_c . This changes both the impedance,

$$\begin{aligned} Z_{tot} &= Z_{in} + \frac{1}{i\omega C} \\ &= 2Z_R \frac{\frac{2Q_i}{\pi} - i \left[\frac{4Q_i^2 \Delta\omega_0}{\pi \omega_0} + \frac{1}{2\omega Z_R C_c} \left(1 + 4Q_i^2 \frac{\Delta\omega_0^2}{\omega_0^2} \right) \right]}{1 + 4Q_i^2 \left(\frac{\Delta\omega_0}{\omega_0} \right)^2}, \end{aligned} \quad (B2)$$

and the resonance frequency to a new value, ω_R :

$$\frac{\Delta\omega_0}{\omega_0} = \frac{2}{\pi} \omega_R Z_R C_c. \quad (B3)$$

Here, we used the fact that $\text{Im}(Z_{tot}) = 0$ at resonance and the assumption that $\frac{Q_i^2}{\pi^2} \gg \frac{1}{4\omega_R^2 C_c^2 Z_R^2}$ which is valid for most resonators with $Q_i \gtrsim 1e5$. Under this assumption, the total impedance at resonance becomes:

$$\begin{aligned} Z_{tot} &= \frac{4Z_R Q_i}{\pi} \frac{1}{1 + \frac{1}{\pi^2} 16Q_i^2 \omega_R^2 Z_R^2 C_c^2} \\ &= \frac{\pi}{4Q_i Z_R \omega_R^2 C_c^2}. \end{aligned} \quad (B4)$$

Equating two general forms of $|S_{11}|$ leads by identification to the desired result [33, 72]:

$$|S_{11}| = \left| \frac{1 - \frac{Z_0}{Z_{tot}}}{1 + \frac{Z_0}{Z_{tot}}} \right| = \left| \frac{1 - \frac{Q_c}{Q_i}}{1 + \frac{Q_c}{Q_i}} \right| \quad (B5)$$

thus

$$Q_c = \frac{\pi}{4Z_0 Z_R \omega_R^2 C_c^2}. \quad (B6)$$

Appendix C. Table of measured resonator parameters

The tabulated values of all measured resonators are shown in table 1. We report the narrow-band (power-dependent) loss tangent $\tan(\delta_p)$, the wide-band (temperature dependent) losses $\tan(\delta_T)$, and the high-power loss tangent (δ_{other}).

Table 1. Measured and inferred values of all resonators data. The device with width $W = 1 \mu\text{m}$ and gap $G = 2 \mu\text{m}$ are used as the base design. Both the reported internal and external quality factors Q_i and Q_c are extracted at average internal photon number $\langle n \rangle = 1$.

W (μm)	G (μm)	L_K ($\frac{\text{pH}}{\square}$)	f_R (GHz)	Z_R (Ω)	Q_i ($\times 10^4$)	Q_c ($\times 10^4$)	$\tan(\delta_P)$ ($\times 10^{-6}$)	$\tan(\delta_T)$ ($\times 10^{-5}$)	δ_{other} ($\times 10^{-6}$)
1	1	9.9	5.98	287	40.3	6.09	4.362	13.43	1.33
1	2	9.3	6.19	310	6.35	4.07	4.547	8.564	15.0
1	5	9.8	6.11	359	65.6	4.01	2.996	6.243	0.748
1	10	9.7	6.09	389	7.87	11.3	3.231	7.766	11.3
1	25	8.8	6.36	411	25.8	3.76	5.583	3.437	2.89
1	50	9.5	6.17	454	4.53	3.27	1.983	4.789	21.6
0.275	2	9.4	5.79	681	47.9	3.50	5.870	17.76	1.66
2	2	9.6	6.10	208	46.9	10.3	2.184	6.181	1.21
5	2	9.9	5.96	123	87.8	16.9	3.074	4.326	0.285
10	2	9.3	5.91	81	44.0	33.6	1.303	2.923	1.19

Appendix D. Derivation of $\langle n \rangle$

To derive the average photon number $\langle n \rangle$ that circulates in the resonator due to an applied power P_{in} , we use the general form of S_{11} , given by equation (B5). Then, the absorbed power by the resonator P_{abs} is given by [73]:

$$\begin{aligned} P_{\text{abs}} &= P_{\text{in}} - |S_{11}|^2 P_{\text{IN}} \\ &= \frac{\hbar\omega_R^2 \langle n \rangle}{Q_i} \end{aligned} \quad (\text{D1})$$

which means that

$$\langle n \rangle = \frac{4Q_i^2}{\hbar\omega_R^2 Q_c} P_{\text{IN}} \quad (\text{D2})$$

as $Q_i = \frac{Q_i Q_c}{Q_i + Q_c}$. To account for reflections due to impedance mismatch, the final result becomes:

$$\langle n \rangle = \frac{Z_0}{Z_R} \frac{4Q_i^2}{\hbar\omega_R^2 Q_c} P_{\text{IN}} \quad (\text{D3})$$

We stress that experimentally most of these values are an approximation, and hence $\langle n \rangle$ is approximate as well.

Appendix E. Phi-factor

Some of the data sets presented in this work show a non-ideal Lorentzian behaviour caused by the resonator's environment, leading to a complex Q_c factor in equation (1). To investigate both the cause of this ϕ -factor and the sporadic 'negative' Q_i observed in the resonator magnetic field spectra (not shown), computational simulations were conducted with the open-source circuit simulator QUCS [38] as shown in table 2. Initially, a perfectly matched sample behaviour was modelled to establish a baseline. Subsequently, controlled perturbations were introduced to various parameters to investigate potential sources contributing to the shoulder-like features observed in the Lorentzian profile governing the magnitude spectrum of the resonator. Finally, we attempt to recreate a ϕ -value corresponding to measurement.

The first aspect investigated is the phase mismatch in the transmission lines between hybrid and sample (*H-S leads*). Here, we varied the cable lengths to induce a phase difference (attributable to electrical length) between the signals emerging from the -3 dB ports of the 180° hybrid. Secondly, we assess the impact of an impedance mismatch in the wirebonds (*Wirebonds*, length and impedance). Notably, this introduces a very large shoulder behaviour in the Lorentzian lineshape, as shown in figure 8(a). Then, we model the non-ideal behaviour of the hybrid by directly altering the phase relation between its output ports (*Hybrid a-e*). This modification did not lead to large changes in the ϕ -factor when using realistic values.

Subsequently, to exclude the influence of the internal quality factor, we vary the resonator's R_R (which directly defines Q_i in QUCS simulations). This is shown in *R resonator a-c*. Even over many orders of magnitude, we observe no appreciable difference in ϕ , indicating that non-ideal Lorentzian behaviour primarily stems from the imperfections introduced in the 180° hybrid component or from wirebonding impedance mismatches. However, we observe the occurrence of a negative Q_i for the higher R_R value, indicating that it may be the ratio between Q_i and Q_c that is of importance. This is only valid when imperfections in the system are present, as shown in the *ideal, high Q_i resonator behaviour*.

To verify the effect of changing coupling factor $g = \frac{Q_i}{Q_c}$, we altered Q_c of two resonators by changing their coupling capacitances (*Coupling C(a)-(b)*), keeping their g consistent with respectively the resonators *R resonator.a* and *R resonator.b*. We conclude that, under similar circumstances, a higher g increases ϕ , which is attributed to a lower coupling to external impedance mismatches. We could not do the same simulations for *R resonator.c* as it is not possible to define a coupling factor for a negative Q_i (which is unphysical). We stress that these negative Q_i s are not physical values, but have to be seen as a convolution of environment and resonator. We show the excellent agreement between fit and simulated data in figure 8 for the simulation *Wirebonds.a*. This confirms in part that especially without a well-known background, getting an accurate value of Q_i for pure reflection type resonators is difficult and leads to inaccuracies not present in

Table 2. Tabulated simulation data of various resonators to uncover the cause of the non-ideal Lorentzian shape of some resonator profiles. The parameters f_r , Q_i , Q_c and ϕ are derived from fitting of simulation.

Variation	Hybrid (°)	H-S leads (mm), (Ω)	Wirebonds (mm), (Ω)	Coupling C (fF), (fF)	R_R (M Ω)	f_r (GHz)	Q_i (1×10^{-5})	Q_c (1×10^{-4})	ϕ (rad)
Ideal	180	100, 50	4, 50	5	100	5.964	10.03	1.14	1.54×10^{-6}
Ideal, high Q_i	180	100, 50	4, 50	5	10×10^{-3}	5.964	1.003×10^{-3}	1.14	3.948×10^{-08}
		100, 50	4, 50	5					
		100, 50	4, 50	5					
Phase mismatch	180	98.3, 50	4, 50	5	100	5.964	-968.1	1.13	1.952×10^{-4}
		100, 50	4, 50	5					
Wirebonds.a	180	100, 50	4, 90	5	100	5.964	-4.921	1.16	5.89×10^{-2}
		100, 50	4, 30	5					
Wirebonds.b	180	100, 50	2.3, 50	5	100	5.964	-1.003×10^{-3}	1.13	1.71×10^{-4}
		100, 50	4, 50	5					
Hybrid.a	167.5	100, 50	4, 50	5	100	5.964	-154.1	1.13	2.264×10^{-4}
		100, 50	4, 50	5					
Hybrid.b	167.9	100, 50	4, 50	5	100	5.964	3040	1.13	2.118×10^{-4}
		100, 50	4, 50	5					
Hybrid.c	170	100, 50	4, 50	5	100	5.964	3.103×10^{-6}	1.14	1.443×10^{-4}
		100, 50	4, 50	5					
Hybrid.d	175	100, 50	4, 50	5	100	5.964	1.205	1.14	3.690×10^{-5}
		100, 50	4, 50	5					
Hybrid.e	185	100, 50	4, 50	5	100	5.964	1.025	1.14	3.689×10^{-5}
		100, 50	4, 50	5					
R resonator.a	170	100, 50	4, 50	5	10	5.964	1.076	1.14	1.582×10^{-4}
		100, 50	4, 50	5					
R resonator.b	170	100, 50	4, 50	5	146	5.964	121.9	1.13	1.438×10^{-4}
		100, 50	4, 50	5					
R resonator.c	170	100, 50	4, 50	5	250	5.964	-36.26	1.14	1.434×10^{-4}
		100, 50	4, 50	5					
Coupling C.a	170	100, 50	4, 50	1.575	100	5.983	10.73	11.3	4.671×10^{-5}
		100, 50	4, 50	1.575					
Coupling C.b	170	100, 50	4, 50	6.046	100	5.958	79.72	0.7783	1.736×10^{-4}
		100, 50	4, 50	6.046					
Combination	170	100, 50	7, 10	5	10	5.964	1.511	1.704	6.016×10^{-1}
		100, 50	4, 90	5					

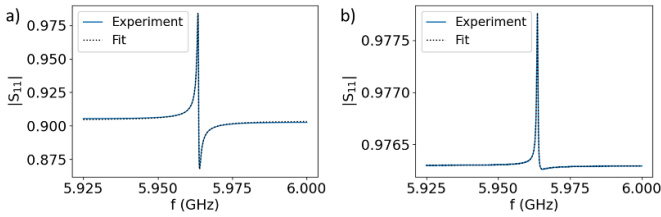


Figure 8. (a) and (b) The simulation of respectively samples *Wirebonds.a* and *Hybrid.a*, showcasing the excellent fit even with a virtual negative internal quality factor.

hanger-mode resonator fitting [4]. The root cause is that with a pure reflection type of resonator, one essentially probes the entire microwave structure in which the resonator is embedded, which can cause constructive interference between the ingoing and outgoing signal. However, since this environment is only minimally power and temperature dependent, we stress that the methodology of using *differences* of Q_i as used in our paper remains valid.

Finally, we combine all potential contributing factors to replicate a similar ϕ as to the measured resonators. Especially the wirebonding impedance mismatch is of prime importance to achieve a realistic result. In practice, such mismatch occurs by e.g. having wirebonds go loose during sample cooldown. Hence, to avoid non-ideal Lorentzian behaviour in these resonators, we suggest to add multiple wirebonds per contact pad. Furthermore, we conclude that the occurrence of a negative Q_i is not directly related to a high ϕ -factor, yet does require a non-symmetric environment. It will only occur at a higher coupling factor.

The custom hybrid S_{11} file, together with the simulation files is available alongside with the data. Note that all the resonator parameters f_r , Q_i , Q_c and ϕ have been obtained from fits to simulation data, using the same fitting algorithm as mentioned in the text [33].

Appendix F. Simulation of the participation ratio

To explain our measured loss spectra, we simulate the participation ratios p_i of the relevant surfaces in the differentially driven co-planar stripline resonators. Generally, there are six interfaces participating in loss-calculations: the metal-air interface (p_{ma}), the metal-surface interface ($p_{substrate}$), the surface-air interface (p_{sa}), the substrate (p_{air}) and the air/vacuum. The total loss tangent of these areas is $\sum_i p_i \tan \delta_i$, where surface type i has a loss tangent δ_i . The participation ratio of a TLS-host volume with relative permittivity ϵ_i is then defined as

$$p_i = \frac{\frac{1}{2} \int_{V_i} \epsilon_i |E|^2 dV}{\frac{1}{2} \int_V \epsilon |E|^2 dV}, \quad (\text{F1})$$

where we calculate the ratio between the energy that is stored in the electric field E in a volume V_i , to the total energy of the electric field threading the resonator. Here, ϵ is the effective permittivity of the entire volume V [18, 59]. These simulations were performed in the Ansys HFSS software package.

Table 3. Simulation parameters of the resonator for different interfaces: metal-air, metal-substrate, substrate-air, substrate and air [15, 74, 75].

Property	Thickness (nm)	Dielectric constant ϵ_i
Metal-air	1.2	54
Metal-substrate	3	11.35
Substrate-air	3	11.35
Substrate	280×10^3	11.35
Air/vacuum	10^6	1

We included the effect of the differential drive in simulations. The simulation parameters are shown in table 3.

ORCID iDs

Ivo P C Cools <https://orcid.org/0000-0001-8822-1470>

Rodrigo M López-Báez <https://orcid.org/0000-0002-9304-0460>

Vittorio Buccheri <https://orcid.org/0009-0009-9354-0869>

Oleg Shvetsov <https://orcid.org/0000-0001-6824-1386>

Nermin Trnjanin <https://orcid.org/0009-0006-6911-5182>

Emil Hogedal <https://orcid.org/0009-0008-1447-5484>

Saroj P Dash <https://orcid.org/0000-0001-7931-4843>

References

- [1] Blais A, Huang R-S, Wallraff A, Girvin S M and Schoelkopf R J 2004 Cavity quantum electrodynamics for superconducting electrical circuits: an architecture for quantum computation *Phys. Rev. A* **69** 062320
- [2] Wallraff A, Schuster D I, Blais A, Frunzio L, Huang R-S, Majer J, Kumar S, Girvin S M and Schoelkopf R J 2004 Strong coupling of a single photon to a superconducting qubit using circuit quantum electrodynamics *Nature* **431** 162–7
- [3] Blais A, Grimsmo A L, Girvin S and Wallraff A 2021 Circuit quantum electrodynamics *Rev. Mod. Phys.* **93** 025005
- [4] McRae C R H, Wang H, Gao J, Vissers M R, Brecht T, Dunsforth A, Pappas D P and Mutus J 2020 Materials loss measurements using superconducting microwave resonators *Rev. Sci. Instrum.* **91** 091101
- [5] Mazin B A 2009 Microwave kinetic inductance detectors: the first decade *AIP Conf. Proc.* **1185** 135–42
- [6] Deng G-W *et al* 2015 Coupling two distant double quantum dots with a microwave resonator *Nano Lett.* **15** 6620–5
- [7] Frey T, Leek P J, Beck M, Blais A, Ihn T, Ensslin K and Wallraff A 2012 Dipole coupling of a double quantum dot to a microwave resonator *Phys. Rev. Lett.* **108** 046807
- [8] Burkard G, Gullans M J, Mi X and Petta J R 2020 Superconductor-semiconductor hybrid-circuit quantum electrodynamics *Nat. Rev. Phys.* **2** 129–40
- [9] Kurizki G, Bertet P, Kubo Y, Mølmer K, Petrosyan D, Rabl P and Schmiedmayer J 2015 Quantum technologies with hybrid systems *Proc. Natl Acad. Sci.* **112** 3866–73
- [10] Xiang Z-L, Ashhab S, You J and Nori F 2013 Hybrid quantum circuits: superconducting circuits interacting with other quantum systems *Rev. Mod. Phys.* **85** 623
- [11] Hays M, Fatemi V, Serniak K, Bouman D, Diamond S, de Lange G, Krogstrup P, Nygård J, Geresdi A and Devoret M H 2020 Continuous monitoring of a trapped superconducting spin *Nat. Phys.* **16** 1103–7

- [12] De Visser P J 2014 Quasiparticle dynamics in aluminium superconducting microwave resonators *PhD Thesis* TUDelft (available at: <https://repository.tudelft.nl/islandora/object/uuid%3Aeae4c9fc-f90d-4c12-a878-8428ee4adb4c>)
- [13] Sage J M, Bolkhovskiy V, Oliver W D, Turek B and Welander P B 2011 Study of loss in superconducting coplanar waveguide resonators *J. Appl. Phys.* **109** 063915
- [14] de Graaf S E, Davidovikj D, Adamyan A, Kubatkin S E and Danilov A V 2014 Galvanically split superconducting microwave resonators for introducing internal voltage bias *Appl. Phys. Lett.* **104** 052601
- [15] Lee J, Lee H, Kim W, Lee J and Kim J 1999 Suppression of coupled-slotline mode on CPW using air-bridges measured by picosecond photoconductive sampling *IEEE Microw. Guid. Wave Lett.* **9** 265–7
- [16] Bothner D, Gaber T, Kemmler M, Koelle D and Kleiner R 2011 Improving the performance of superconducting microwave resonators in magnetic fields *Appl. Phys. Lett.* **98** 102504
- [17] Nulens L et al 2023 Catastrophic magnetic flux avalanches in NbTiN superconducting resonators *Commun. Phys.* **6**
- [18] Wenner J et al 2011 Surface loss simulations of superconducting coplanar waveguide resonators *Appl. Phys. Lett.* **99** 113513
- [19] Samkharadze N, Bruno A, Scarlino P, Zheng G, DiVincenzo D, DiCarlo L and Vandersypen L 2016 High-kinetic-inductance superconducting nanowire resonators for circuit QED in a magnetic field *Phys. Rev. Appl.* **5** 044004
- [20] Yu C X et al 2021 Magnetic field resilient high kinetic inductance superconducting niobium nitride coplanar waveguide resonators *Appl. Phys. Lett.* **118** 054001
- [21] Amin K R, Ladner C, Jourdan G, Hentz S, Roch N and Renard J 2022 Loss mechanisms in tin high impedance superconducting microwave circuits *Appl. Phys. Lett.* **120** 164001
- [22] Kirby K W 2008 Processing of sapphire surfaces for semiconductor device applications
- [23] Burton M C, Beebe M R, Yang K, Lukaszew R A, Valente-Feliciano A-M and Reece C 2016 Superconducting nbtin thin films for superconducting radio frequency accelerator cavity applications *J. Vac. Sci. Technol. A* **34** 021518
- [24] Niepce D 2020 Superinductance and fluctuating two-level systems: loss and noise in disordered and non-disordered superconducting quantum devices *PhD Thesis* Chalmers Tekniska Hogskola
- [25] Mahashabde S, Otto E, Montemurro D, de Graaf S, Kubatkin S and Danilov A 2020 Fast tunable high-Q-factor superconducting microwave resonators *Phys. Rev. Appl.* **14** 044040
- [26] Pobell F 2007 *Matter and Methods at low Temperatures* (Springer Science & Business Media)
- [27] Krinner S, Storz S, Kurpiers P, Magnard P, Heinsoo J, Keller R, Lütolf J, Eichler C and Wallraff A 2019 Engineering cryogenic setups for 100-qubit scale superconducting circuit systems *EPJ Quantum Technol.* **6** 1103–7
- [28] Kurpiers P, Walter T, Magnard P, Salathe Y and Wallraff A 2017 Characterizing the attenuation of coaxial and rectangular microwave-frequency waveguides at cryogenic temperatures *EPJ Quantum Technol.* **4** 1–15
- [29] Barends R et al 2011 Minimizing quasiparticle generation from stray infrared light in superconducting quantum circuits *Appl. Phys. Lett.* **99** 113507
- [30] Milliken F P, Rozen J R, Keefe G A and Koch R H 2007 50 Ohm characteristic impedance low-pass metal powder filters *Rev. Sci. Instrum.* **78** 024701
- [31] Lukashenko A and Ustinov A V 2008 Improved powder filters for qubit measurements *Rev. Sci. Instrum.* **79** 014701
- [32] Khalil M S, Stoutimore M, Wellstood F and Osborn K 2012 An analysis method for asymmetric resonator transmission applied to superconducting devices *J. Appl. Phys.* **111** 054510
- [33] Probst S, Song F, Bushev P A, Ustinov A V and Weides M 2015 Efficient and robust analysis of complex scattering data under noise in microwave resonators *Rev. Sci. Instrum.* **86** 024706
- [34] Kudra M, Biznárová J, Roudsari A F, Burnett J J, Niepce D, Gasparinetti S, Wickman B and Delsing P 2020 High quality three-dimensional aluminum microwave cavities *Appl. Phys. Lett.* **117** 070601
- [35] Doyle S, Mauskopf P, Naylon J, Porch A and Duncombe C 2008 Lumpes *J. Low Temp. Phys.* **151** 530–6
- [36] Megrant A et al 2012 Planar superconducting resonators with internal quality factors above one million *Appl. Phys. Lett.* **100** 113510
- [37] Geerlings K L 2013 Improving coherence of superconducting qubits and resonators *PhD Thesis* Yale University (available at: <https://ui.adsabs.harvard.edu/abs/2013PhDT.....252G>)
- [38] Brinson M, Crozier R, Novak C, Roucaries B, Schreuder F and Torri G B 2015 Qucs: an introduction to the new simulation and compact device modelling features implemented in release 0.0.19/0.0.19 Src2 of the popular GPL circuit simulator 1–46
- [39] Cools I 2022 Basic mw analysis fitting and controlling software
- [40] Annunziata A J, Santavica D F, Frunzio L, Catelani G, Rooks M J, Frydman A and Prober D E 2010 Tunable superconducting nanoinductors *Nanotechnology* **21** 445202
- [41] Yang X, You L, Zhang L, Lv C, Li H, Liu X, Zhou H and Wang Z 2018 Comparison of superconducting nanowire single-photon detectors made of NbTiN and NbN thin films *IEEE Trans. Appl. Supercond.* **28** 1–6
- [42] Zichi J 2019 NbTiN for improved superconducting detectors *PhD Thesis* KTH Royal Institute of Technology
- [43] Thoen D J, Bos Boy Gustaaf Cornelis, Haalebos E A F, Klapwijk T M, Baselmans J J A and Endo A 2017 Superconducting NbTiN thin films with highly uniform properties over a \varnothing 100 mm wafer *IEEE Trans. Appl. Supercond.* **27** 1–5
- [44] Weber S J, Murch K W, Slichter D H, Vijay R and Siddiqi I 2011 Single crystal silicon capacitors with low microwave loss in the single photon regime *Appl. Phys. Lett.* **98** 172510
- [45] Burnett J, Bengtsson A, Niepce D and Bylander J 2018 Noise and loss of superconducting aluminium resonators at single photon energies *J. Phys.: Conf. Ser.* **969** 012131
- [46] Burnett J, Faoro L and Lindström T 2016 Analysis of high quality superconducting resonators: consequences for TLS properties in amorphous oxides *Supercond. Sci. Technol.* **29** 044008
- [47] Phillips W A 1987 Two-level states in glasses *Rep. Prog. Phys.* **50** 1657
- [48] Nsanzineza I 2016 Vortices and quasiparticles in superconducting microwave resonators *PhD Thesis* Syracuse University
- [49] Grünhaupt L, Maleeva N, Skacel S T, Calvo M, Levy-Bertrand F, Ustinov A V, Rotzinger H, Monfardini A, Catelani G and Pop I M 2018 Loss mechanisms and quasiparticle dynamics in superconducting microwave resonators made of thin-film granular aluminum *Phys. Rev. Lett.* **121** 117001
- [50] de Graaf S E, Faoro L, Burnett J, Adamyan A A, Tzalenchuk A Y, Kubatkin S E, Lindström T and Danilov A V 2018 Suppression of low-frequency charge

- noise in superconducting resonators by surface spin desorption *Nat. Commun.* **9** 1143
- [51] Pappas D P, Vissers M R, Wisbey D S, Kline J S and Gao J 2011 Two level system loss in superconducting microwave resonators *IEEE Trans. Appl. Supercond.* **21** 871–4
- [52] Abdo B, Segev E, Shtempluck O and Buks E 2006 Nonlinear dynamics in the resonance line shape of NbN superconducting resonators *Phys. Rev. B* **73** 134513
- [53] Gao J, Daal M, Vayonakis A, Kumar S, Zmuidzinas J, Sadoulet B, Mazin B A, Day P K and Leduc H G 2008 Experimental evidence for a surface distribution of two-level systems in superconducting lithographed microwave resonators *Appl. Phys. Lett.* **92** 152505
- [54] Coumou P C J J 2015 Electrodynamics of strongly disordered superconductors *PhD Thesis* Technische Universiteit Delft (available at: <https://repository.tudelft.nl/islandora/object/uuid%3Aad01901d-511f-4496-ae66-301d0db92caa>)
- [55] Gao J 2008 The physics of superconducting microwave resonators *PhD Thesis* California Institute of Technology
- [56] Arzeo M, Lombardi F and Bauch T 2014 Microwave losses in MgO, LaAlO₃ and (La_{0.3}Sr_{0.7})(Al_{0.65}Ta_{0.35})O₃ dielectrics at low power and in the millikelvin temperature range *Appl. Phys. Lett.* **104** 212601
- [57] McRae C R H, Béjanin J H, Earnest C T, McConkey T G, Rinehart J R, Deimert C, Thomas J P, Wasilewski Z R and Mariantoni M 2018 Thin film metrology and microwave loss characterization of indium and aluminum/indium superconducting planar resonators *J. Appl. Phys.* **123** 205304
- [58] Lahtinen V and Möttönen M 2020 Effects of device geometry and material properties on dielectric losses in superconducting coplanar-waveguide resonators *J. Phys.: Condens. Matter* **32** 405702
- [59] Niepce D, Burnett J J, Latorre M G and Bylander J 2020 Geometric scaling of two-level-system loss in superconducting resonators *Supercond. Sci. Technol.* **33** 025013
- [60] Vendik I B, Gubina M N, Deleniv A N and Kholodnyak D V 1997 Distribution of current, surface impedance and damping in superconductor coupled microstriplines *Techn. Phys.* **42** 196–201
- [61] Deleniv A, Gubina M, Kholodnyak D and Vendik I 1998 Model of high-temperature superconducting coupled microstrip lines on anisotropic sapphire substrate *Int. J. RF Microw. Comput.-Aided Eng.* **8** 375–85
- [62] Müller M et al 2022 Magnetic field robust high quality factor nbtin superconducting microwave resonators *Mater. Quantum Technol.* **2** 015002
- [63] Read A P, Chapman B J, Lei C U, Curtis J C, Ganjam S, Krayzman L, Frunzio L and Schoelkopf R J 2023 Precision measurement of the microwave dielectric loss of sapphire in the quantum regime with parts-per-billion sensitivity *Phys. Rev. Appl.* **19** 034064
- [64] Tinkham M 2004 *Introduction to Superconductivity Secondedn* 2nd edn (Dover Publications)
- [65] Sidorova M, Semenov A D, Hübers H-W, Gyger S, Steinhauer S, Zhang X and Schilling A 2021 Magnetoconductance and photoresponse properties of disordered NbTiN films *Phys. Rev. B* **104** 184514
- [66] Mironov A Y, Silevitch D M, Proslir T, Postolova S V, Burdastyh M V, Gutakovskii A K, Rosenbaum T F, Vinokur V V and Baturina T I 2018 Charge Berezinskii-Kosterlitz-Thouless transition in superconducting nbtin films *Sci. Rep.* **8** 4082
- [67] Yu L, Newman N and Rowell J 2002 Measurement of the coherence length of sputtered nb/sub 0.62/ti/sub 0.38/n thin films *IEEE Trans. App. Supercond.* **12** 1795–8
- [68] Pearl J 1964 Current distribution in superconducting films carrying quantized fluxoids *Appl. Phys. Lett.* **5** 65–66
- [69] Kroll J et al 2019 Magnetic-field-resilient superconducting coplanar-waveguide resonators for hybrid circuit quantum electrodynamics experiments *Phys. Rev. Appl.* **11** 064053
- [70] Shetvsov O, Ankit A, Buccheri V, Cools I P C, Trnjanin N and Geresdi A 2025 Strong coupling between Andreev bound states and a high impedance lumped-element resonator (arXiv:2502.09243)
- [71] Werthamer N R, Helfand E and Hohenberg P C 1966 Temperature and purity dependence of the superconducting critical field, III. electron spin and spin-orbit effects *Phys. Rev.* **147** 295–302
- [72] Pozar D M 2011 *Microwave Engineering* 4th edn (Wiley)
- [73] Bruno A, De Lange G, Asaad S, Enden K L, Langford N and DiCarlo L 2015 Reducing intrinsic loss in superconducting resonators by surface treatment and deep etching of silicon substrates *Appl. Phys. Lett.* **106** 182601
- [74] Kaiser C, Skacel S T, Wünsch S, Dolata R, Mackrodt B, Zorin A and Siegel M 2010 Measurement of dielectric losses in amorphous thin films at gigahertz frequencies using superconducting resonators *Supercond. Sci. Technol.* **23** 075008
- [75] Clima S, Pourtois G, Hardy A, Van Elshocht S, Van Bael M K, De Gendt S, Wouters D J, Heyns M and Kittl J A 2010 Dielectric response of TaO₅, Nb₂O₅, and NbTaO₅ from first-principles investigations *J. Electrochem. Soc.* **157** G20